Response to a Steady Poleward Outflow. Part II: Oscillations and Eddies

THEODORE S. DURLAND

College of Oceanic and Atmospheric Sciences, Oregon State University, Corvallis, Oregon

MICHAEL A. SPALL AND JOSEPH PEDLOSKY

Woods Hole Oceanographic Institution, Woods Hole, Massachusetts

ABSTRACT

A conceptually simple model is presented for predicting the amplitude and periodicity of eddies generated by a steady poleward outflow in a 1½-layer β-plane formulation. The prediction model is rooted in linear quasigeostrophic dynamics but is capable of predicting the amplitude of the β plume generated by outflows in the nonlinear range. Oscillations in the plume amplitude are seen to represent a near-zero group velocity response to an adjustment process that can be traced back to linear dynamics. When the plume-amplitude oscillations become large enough so that the coherent β plume is replaced by a robust eddy field, the eddy amplitude is still constrained by the plume-amplitude prediction model. The eddy periodicity remains close to that of the predictable, near-zero group-velocity linear oscillations.

Striking similarities between the patterns of variability in the model and observations south of Indonesia's Lombok Strait suggest that the processes investigated in this study may play an important role in the generation of the observed eddy field of the Indo-Australian Basin.

1. Introduction

An energetic eddy field has been observed between 9°S and 16°S in the eastern Indian Ocean between Indonesia and Australia (Bray et al. 1997; Feng and Wijffels 2002, hereafter FW). We will follow Yu and Potemra (2006) in referring to this region as the Indo-Australian Basin (IAB). The eddy field is coincident with the South Equatorial Current (SEC), which derives much of its source waters from the Indonesian Throughflow (ITF). Most of the throughflow waters enter the IAB at its eastern boundary, in a predominantly zonal flow through Timor Passage (11.5°S, 123°E) and Ombai Strait (8.5°S, 125°E). Of the major throughflow channels, the farthest west is Lombok Strait (9°S, 116°W), through which roughly 25% of the annual mean ITF empties into the Indian Ocean in a dominantly poleward flow. (In this paper, "poleward" will refer to a meridional flow directed away from the equator, whether in the Southern or Northern Hemi-

sphere.) Fig. 1 shows the IAB with the major ITF passages and a schematic of the major currents in the vicinity.

FW analyzed 6 yr of satellite altimetry data (October 1992 through December 1998) and showed that during this period and in the region of interest

- the maximum intraseasonal variability in sea surface height (SSH) occurred during the second half of the calendar year: during and following the time of ITF and SEC maxima;
- the maximum standard deviation of SSH was located at about 12°S, 110°E: roughly 3° south and 6° west of the mouth of Lombok Strait;
- dominant periodicity at the point of maximum variance ranged between 40 and 80 days.

The standard deviation of intraseasonal SSH variability over the 6-yr period is contoured in Fig. 1 (from FW, Fig. 2).

Not having adequate data to address barotropic stability, FW used hydrographic climatology to analyze the baroclinic instability of the SEC, employing a classical analysis for continuous stratification. They concluded that only during July and August, when the ITF and SEC are at their strongest, is the baroclinic instability growth

Corresponding author address: Theodore S. Durland, College of Oceanic and Atmospheric Sciences, Oregon State University, Corvallis, OR 97331.
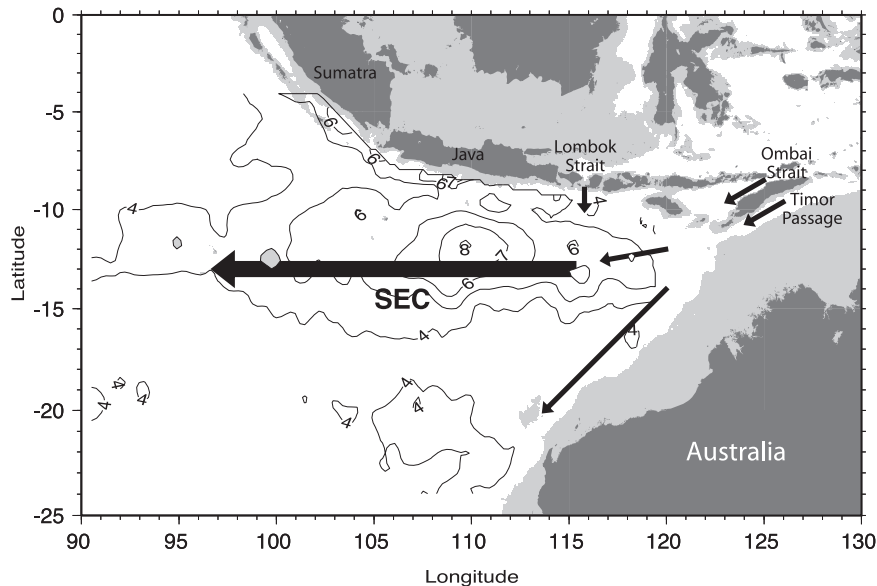E-mail: tdurland@whoi.edu

FIG. 1. Site map of the Indo-Australian Basin (adapted from FW, Figs. 1 and 2). Arrows indicate the major Indonesian Throughflow passages and the major basin currents, most importantly the SEC. Contours are of the standard deviation in intraseasonal SSH variability over the 6-yr period from October 1992 through December 1998.

rate fast enough to produce the observed SSH variability. The continued high variability seen during October through December was presumed to be a free wave remnant of the strong austral winter generation season.

We note that Fig. 3a in FW shows a SSH standard deviation pattern during the January–March composite months that is similar to the pattern seen during the composite months of July–December and weaker by only about 30%. The location of the main peak in standard deviation is shifted inshore by about 1° from the location of the July–December peak. During the composite months April through June (FW, Fig. 3b) the variability is weaker yet, but a similar standard deviation pattern is still visible. FW's Fig. 7a shows a wavelet analysis of the SSH anomalies at 12°S, 110°E. The most robust periodicity peaks are seen in the second half of 1994, 1995, and 1997, but a peak in the 40–80-day period band can be seen to continue almost unbroken throughout the entire 6-yr record.

Yu and Potemra (2006) modeled the IAB intraseasonal variability with a 4 ½-layer model of the Indian Ocean, forced by realistic surface fluxes and by specified ITF transports through Timor Passage, Ombai Strait, and Lombok Strait. They found the barotropic conversion terms to be slightly stronger than the baroclinic conversion terms and concluded that the IAB eddies owe their existence to a mixed instability process. The region of maximum conversion in both cases was found to be closely linked to the Lombok Strait outflow. Elim-

inating the Lombok Strait outflow greatly decreased the offshore variability. Diverting the Lombok transport through Ombai Strait renewed the variability but shifted the region of maximum variance south and east. The inference was that the instability depends on the strength of the SEC, and that, in the realistic case, the Lombok Strait outflow merely provides the extra contribution to the SEC necessary to push it over the instability threshold. We will present model results suggesting that an additional mechanism, not previously considered, contributes to the importance of the Lombok Strait outflow for the IAB variability pattern.

Nof et al. (2002) ascribed the IAB variability to a process of eddy shedding from the steady, westward-flowing Timor Passage branch of the ITF as it changes direction to follow the Australian coast southwestward. Eddies are observed to the east of Lombok Strait that may indeed be attributable to the Timor Passage outflow, but the location of maximum variability and the analysis of Yu and Potemra (2006) strongly suggest that the poleward Lombok Strait outflow plays a major role in establishing the IAB variability pattern. Pichevin and Nof (1997, hereafter PN) present a theoretical model of eddy shedding from a steady poleward outflow, and Nof (2005) provides an updated analysis of the model with qualitatively similar results. PN and Nof (2005) use a 1½-layer model in which a light fluid exits a channel mouth into a basin of heavier fluid. The upper-layer thickness vanishes at the edge of any current or eddies

generated by the outflow, so that the eddies are isolated lenslike features. The poleward outflow turns eastward to follow the coast in the direction of Kelvin wave propagation, but an imbalance of zonal momentum causes a ballooning of the outflow region, which eventually detaches into a westward-propagating anticyclonic eddy when the balloon gets too large. The eddy shedding period is thus inversely proportional to the outflow volume flux and approaches infinity as the volume flux approaches zero.

In a 1½-layer shallow-water-equation model with a nonzero upper-layer thickness everywhere, we have found that the response to a steady poleward outflow exhibits some important differences from the response found by PN, but it bears a striking resemblance to the observations of FW. Figure 2 shows three snapshots of the upper-level thickness contours for three progressively stronger values of outflow velocity. The poleward outflow, at the latitude of Lombok Strait, was started with a 20-day taper to minimize gravity wave noise and held steady thereafter. The snapshots were taken 1 yr after initiation of the outflow.

At the top of each panel is shown the Froude number (Fr) and the Reynolds number (Re) of the model outflow (see section 2 for definitions). The top panel of Fig. 2, with the weakest outflow, represents essentially linear dynamics; the bottom panel is for an outflow velocity of about 54 cm s^{-1} (Fr = 0.2); and the middle panel represents an intermediate case. In a 2 + year pressure-gauge deployment calibrated by repeat ADCP sections, Chong et al. (2000) found southward currents in the Lombok Strait in the 1–2 m s^{-1} range for extended periods during the austral winter months. The channel mouth in the model is one deformation radius (110 km) in width, which is on the order of the strait width at which the above currents were measured (80 km). The outflow volume flux in the bottom panel of Fig. 2 is therefore well within the range of volume flux found at Lombok. (Note that the mouth of Lombok Strait is somewhat narrower, variously reported as between 30 and 40 km.)

Each panel of Fig. 2 shows a coastal-trapped current carrying most of the outflow volume transport to the east (as in PN). This current is set up by a Kelvin wave at the initiation of the outflow, and the steady current retains the cross-shore Kelvin wave structure. We therefore refer to this feature as the "Kelvin current." To the west of the channel mouth, a plume-like structure propagates westward at the local long Rossby wave speed. This feature is generated in response to the crossing of planetary vorticity contours as the outflow feeds the Kelvin current, and we will henceforth refer to it as the "β plume."

In all panels of Fig. 2 we also see smaller-scale oscillations superimposed on the β plumes. These oscilla-

tions increase in amplitude with increasing outflow velocity, but their zonal spacing and periodicity (not shown) change little between the essentially linear oscillations in the top panel and the nonlinear eddies in the bottom one. This is in marked contrast to the behavior of the lens-type model of PN, in which the eddies do not shed to the west until they reach a minimum size. In our model the underlying oscillation appears to be always present, however weakly, and to grow in strength as the forcing increases, eventually developing into robust eddies. These results are in agreement with the observations of FW discussed above, in which the zonal pattern of variability and essential periodicity remain relatively constant even during the weakly forced austral summer months.

The upper panel of Fig. 3 shows contours of the standard deviation in the model's upper-layer thickness, measured over a period of about 1 yr. The lower panel shows a time series of the normalized upper-layer thickness deviation over the same period, measured at the location of maximum variance. The pattern in the top panel shows a striking similarity to Figs. 3c and 3d in FW, with the main variability peak located almost 3° offshore and 10° west of the outflow mouth and a secondary peak to the east of the outflow mouth. In our weakly forced case, the variability to the east of the mouth is easily recognized as linear short Rossby waves superimposed on the Kelvin current. They appear to increase in amplitude and eastward group velocity with increasing channel flow. In this paper we will be primarily concerned with the more robust westward-propagating eddies, but we note here that the variability to the east of the outflow is consistent with observations. A secondary variability peak east of Lombok Strait is clearly visible in FW, Fig. 3d, for the October–December composite months, although it is less apparent in the annual composite (our Fig. 1). The layer thickness oscillations seen in the lower panel of Fig. 3 have a periodicity in the 75–80-day range, again consistent with the observations of FW.

Yu and Potemra (2006) have asserted that a mixed barotropic–baroclinic instability process is responsible for the IAB eddy field. The 1 ½-layer model that we present does not support baroclinic instability and it does not contain a preexisting alongshore current (SEC). Nevertheless, the coincidence of the model's spatial and temporal patterns of variability with those of the observations leads us to offer the dynamics of the steady meridional outflow as a potentially important contributor to the generation of the IAB eddies. In addition, the differences between the behavior of the finite-thickness-layer model and the lens-type model of PN make the understanding of the former an important step toward
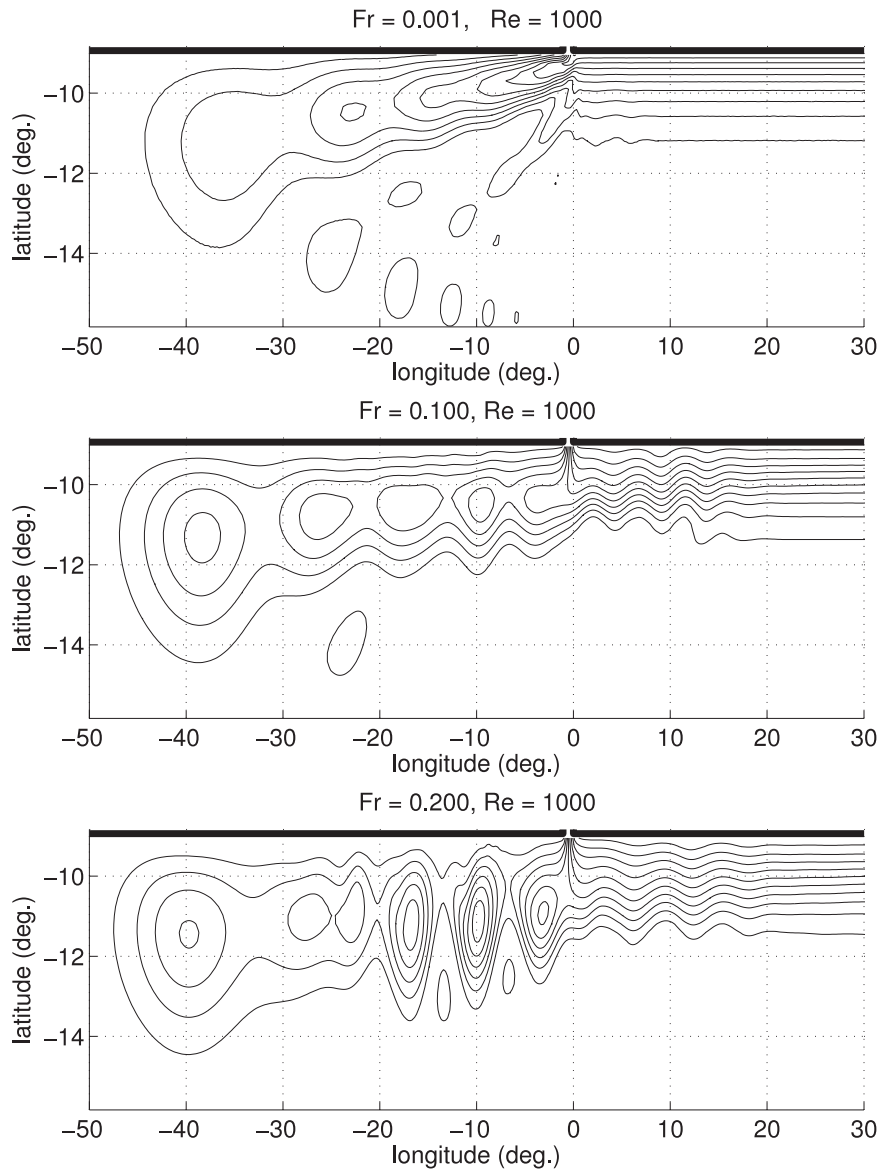
FIG. 2. Contours of upper-layer thickness deviation δh in 1½-layer model at 1 yr after initiation of outflow.

completing the general theory of steady outflows. The poleward outflow, in particular, has applications in other parts of the world, such as the Yucatan Channel, where the Gulf Stream enters the Gulf of Mexico (addressed by PN), and Amchitka Pass in the Aleutian Islands, where a northward-flowing branch of the Alaskan Stream enters the Bering Sea.

The goal of this paper is to demonstrate that much of the behavior of the nonlinear 1½-layer model can be understood in terms of a continuous progression from linear dynamics. A conceptually simple model for predicting the plume amplitude is presented. It is rooted in linear, quasigeostrophic (QG) dynamics but performs

well for a wide range of outflow velocities and latitudes. Surprisingly, when the small-scale plume-amplitude oscillations grow to the extent that the coherent β plume is replaced by a robust eddy field, the eddy amplitudes are still constrained by the same plume-amplitude predictor.

In this paper we present numerical solutions to the shallow-water equations (SWEs), both linear and nonlinear. The mathematical formalism, problem formulation, and numerical model details are found in section 2. Section 3 presents solutions to the linear equations, beginning with a summary of the linear QG solution to the equivalent problem. This problem was solved in a companion paper, Durland et al. (2009, hereafter referred
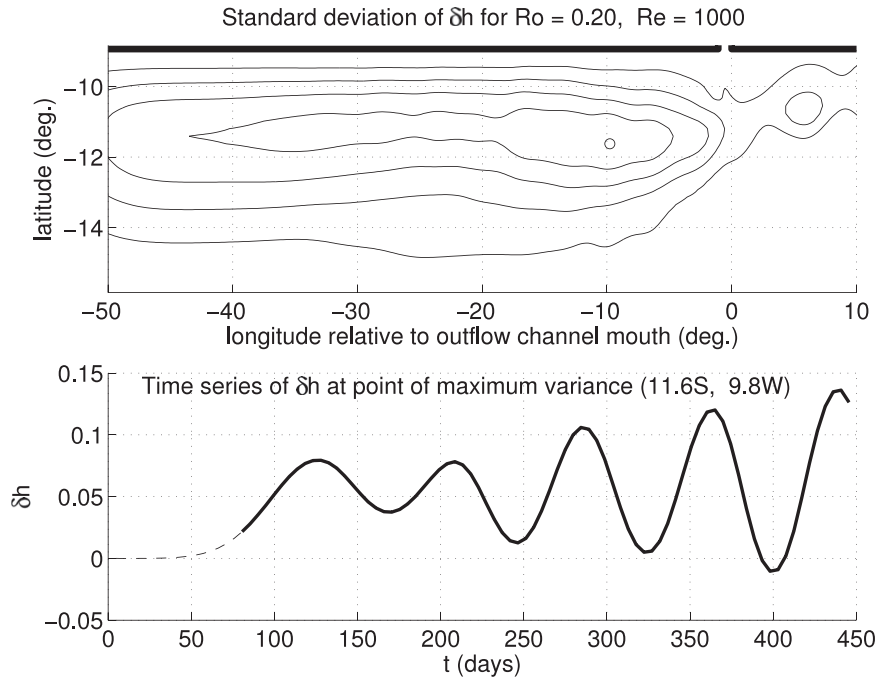
Standard deviation of δh for Ro = 0.20, Re = 1000

FIG. 3. Upper-layer thickness variability for Ro = 0.2, Re = 1000. (top) Spatial pattern of standard deviation in upper-layer thickness. (bottom) Time series of layer thickness deviation (δh) at point of maximum variability. Solid part of curve denotes time period over which variability in (top) is measured.

to as DPS), and the important result connecting the two papers is the concept of plume evolution. At a given longitude, the β plume's cross-shore thickness-deviation profile begins with a low peak far offshore. As time passes, this peak grows and migrates onshore monotonically, asymptoting to the maximum thickness deviation imposed at the outflow channel mouth.

In the remainder of section 3, we show that the QG plume-evolution model does a good job of predicting the mean SWE plume evolution even at low latitudes, but the small-scale plume oscillations we noted in Fig. 2 are peculiar to the low-latitude SWE solutions. These oscillations are found to occur at the latitude-dependent frequency associated with zero group-velocity Rossby waves, and they are shown to be associated with the β effect's ''squeezing'' of the Kelvin wave as it rounds the corner upon exiting the channel mouth.

Section 4 presents the nonlinear SWE solutions and introduces the concept of arrested plume evolution. We see that the mean plume structure evolves similarly to the linear plume but only up to a point that is inversely proportional to the outflow strength. A simplified mechanism is proposed to explain this behavior and is found to produce a good plume-amplitude predictor. The plume-amplitude oscillations are in general stronger than in the linear model, but they are found to retain a periodicity

that differs little from the linear model. The onset of robust eddies is shown to occur near an outflow volume-flux threshold, and the eddy amplitudes are shown to be well predicted by the plume-amplitude model. Section 5 presents a brief summary and suggestions for future research.

2. Model

We work with the nondimensional SWE on the β plane:

$$\partial_t u + u\partial_x u + v\partial_y u - fv + \partial_x h = E_h\nabla^2 u, \qquad (1)$$

$$\partial_t v + u\partial_x v + v\partial_y v + fu + \partial_y h = E_h\nabla^2 v, \qquad (2)$$

$$\partial_t h + \partial_x(hu) + \partial_y(hv) = 0, \qquad (3)$$

with x and y being the eastward and northward Cartesian coordinates, u and v the zonal and meridional components of velocity, f the Coriolis parameter, and h the upper-layer thickness. The normalization is $(x^*, y^* - y_0) = (x, y)L_d$, $(u^*, v^*) = (u, v)c$, $t^* = tf_0^{-1}$, $h^* = hH_0$, and $f^* = f_0 + \beta_0(y^* - y_0) = ff_0$, where stars denote dimensional variables. Here H_0 is the undisturbed upper-layer thickness and $c = \sqrt{g'H_0}$ is the linear gravity wave speed, with g' being the reduced gravity of the 1½-layer

system. Since our preliminary experiments lead us to expect near-boundary solutions, we set our reference latitude at the outflow, with f_0 being the Coriolis parameter and $L_d = c/f_0$ the deformation radius at the outflow latitude θ_0. The dimensional meridional coordinate at the outflow latitude is y_0, and β_0 is the meridional derivative of f^* at the outflow latitude. Here $E_h = A_h/(f_0 L_d^2)$ is the horizontal Ekman number based on the deformation radius, with A_h being the turbulent viscosity coefficient. Note that we are considering an adiabatic system with no thickness diffusion.

In low-latitude scenarios, where f changes significantly within the flow regime, certain aspects of the plume might not be best characterized by the boundary-latitude deformation radius. In these cases we will calculate such things as Rossby wave speeds and cutoff frequencies based on an ''effective latitude'' θ_α associated with an effective meridional coordinate residing within the plume:

$$y_\alpha = y_0 + \alpha L_d, \qquad (4)$$

where α is a dimensionless ratio. Expressing the dynamics in terms of a single latitude is an imperfect representation of the low-latitude β plane, and different aspects of the plume may require different values of α in (4).

We focus on the specific outflow conditions of a uniform velocity, and a uniform potential vorticity (PV) that is equal to the ambient basin PV at the channel mouth. Given that the depth of the Lombok Strait sill (≈ 300 m) is roughly equal to a reasonable choice of undisturbed upper-layer thickness for the IAB (Qiu et al. 1999), and given the expected high-Reynolds-number nature of the channel flow, the above specifications are appropriate for a first look at the problem. Unless stated otherwise, we will use an outflow channel width of one deformation radius. This is somewhat wider than the Lombok Strait (variously reported as 1/4 to 1/3 the local deformation radius), but it is a convenient size for the generic problem. Some effects of varying the channel width will be addressed.

With the given normalization, the deformation-radius Rossby number is equal to the characteristic nondimensional velocity. Because the deformation radius is clearly the dynamically important length scale (see Fig. 2), the Rossby number of the problem is equal to the Froude number:

$$\text{Ro} = V_0/c = \text{Fr}, \qquad (5)$$

where V_0 is the dimensional, uniform outflow velocity. We will henceforth use the Rossby number to describe the strength of the outflow, and we will consider flows ranging from Ro $\ll 1$ (the linear limit) up to Ro = $O(1)$. In dimensional examples we base L_d and the relation between Ro and V_0 on $c = 2.7$ m s^{-1}. The Reynolds number of the flow is

$$\text{Re} = \text{Ro}/E_h, \qquad (6)$$

and the nondimensional derivative of the Coriolis parameter is

$$\beta = \frac{\beta_0 L_d^2}{c}. \qquad (7)$$

It will often be convenient to refer to the upper-layer thickness deviation, which is simply

$$\delta h = h - 1. \qquad (8)$$

Our domain is confined between zonal boundaries to the north and to the south. The fluid is quiescent to begin with, and at $t = 0$ we initiate a poleward flow through a channel mouth of width w on the equatorward boundary of the domain. The boundary condition at the reference latitude y_0 is

$$v(x, y = y_0, t) = \begin{cases} \text{Ro } T(t), & |x| < w/2 \\ 0, & |x| > w/2, \end{cases} \qquad (9)$$

where

$$T(t) = \begin{cases} 0, & t < 0 \\ O(1), & t > 0 \\ 1, & t \gg 1 \end{cases} \qquad (10)$$

and Ro is the Rossby number, as discussed above. The distance between the zonal boundaries is large enough so that the flow cannot ''feel'' the poleward boundary during the integration time, as is appropriate for a model of the IAB eddies.

The numerical model uses second-order, centered spatial differences on a staggered C grid, and a leapfrog time evolution scheme. The nonlinear calculations use an energy-conserving advection scheme (Sadourny 1975). The grid resolution is one-fifth of the deformation radius, and limited calculations at double and quadruple this resolution showed the solutions to be well converged at the coarser resolution. A 1/4-sine wave taper from $t = 0$ is included in $T(t)$ to minimize inertia–gravity wave generation. The zonal extent of the domain is chosen so that long Rossby waves generated at the outflow do not have time to reach the western boundary, and Kelvin waves do not have time to reflect from the eastern boundary and return to the longitude of the channel mouth during the integration.

Figures 2 and 3 were generated from a Southern Hemisphere perspective to emphasize our comparisons

with the IAB eddy field and to facilitate direct comparison with FW's Fig. 3. In the remaining figures, we will represent Northern Hemisphere outflows for ease of comparison with the results of PN. The difference between the two perspectives is merely a reflection through the equator. When it is desirable to cite specific dimensional quantities, we will typically use those relevant to the Lombok Strait outflow while retaining a Northern Hemisphere representation.

3. Linear solutions

Figure 2 shows that two important elements of the nonlinear solutions, the establishment of the β plume and the existence of smaller-scale oscillations in the plume strength, are foreshadowed by the linear solution. This section is devoted to understanding these features in the linear, inviscid model (Ro $\ll$ 1, $E_h = 0$) prior to investigating the more complicated nonlinear behavior.

a. QG–midlatitude plume

At midlatitudes and long time scales, we expect that the SWE will be well approximated by the quasigeostrophic formulation, and the linear QG solution for a switched-on poleward outflow is presented in DPS. The QG β-plane assumption that $(f^* - f_0)/f_0 \ll 1$ throughout the domain does not hold at low latitudes, but we will see that important insights gained from the QG solution remain valid in the SWE solution at the latitude of Lombok Strait.

The take-home message from DPS is that the Kelvin current sets up rapidly at the onset of the outflow, and the β plume is generated by the Rossby adjustment of the Kelvin current's western front where the outflow must cross planetary vorticity contours to feed the coastal current. Each individual Fourier component of the Kelvin current's meridional spectrum propagates westward at its particular group velocity, which decreases with increasing meridional wavenumber. At a given meridian west of the channel mouth, the cross section of the plume constantly evolves (as new wave fronts pass through) toward an eastward-flowing Kelvin current structure on which is superimposed a δ-function westward current at the coast. The peak in the pressure signal starts off small and far offshore, and as time passes it grows larger and migrates toward shore monotonically, asymptoting to the maximum pressure anomaly imposed at the outflow. At intermediate stages of the evolutionary process, additional pressure peaks appear offshore, but these are much smaller than the primary, nearshore peak and we will not be concerned with them.

The "long-wave approximation" developed in DPS quantifies the plume evolution in a channel of width L:

$$\psi_L(x,y,t) = \text{Ro}\, w \frac{2}{L} \sum_{n=1}^{N(\beta t/x)} \frac{l_n}{l_n^2 + 1} \sin l_n y, \quad (11)$$

where

$$\frac{L}{\pi}\sqrt{-\left(\frac{\beta t}{x} + 1\right)} - 1 \le N < \frac{L}{\pi}\sqrt{-\left(\frac{\beta t}{x} + 1\right)} \quad (12)$$

[identical to (33) and (34) in DPS]. Here ψ_L is the QG streamfunction; Ro and w the outflow Rossby number and channel width, respectively; and $l_n \equiv n\pi/L$ is a meridional wavenumber. The quantity $l_n/(l_n^2 + 1)$ is the mode-n Fourier sine transform of e^{-y}, the Kelvin current's cross-shore structure. The β plume evolves by successively adding higher wavenumber members of the Kelvin current's spectrum to its own meridional spectrum. At any given time, a snapshot of the plume (e.g., top panel of Fig. 2) also reflects the evolutionary process, with the western front of the plume representing an early stage (broad offshore scale and small peak) and more eastward locations representing later stages (larger peak closer to shore).

Note that time enters into (11) and (12) only in combination with β. The quantity βt represents the distance the fastest Rossby waves have traveled (i.e., the western front of the plume) in units of the local deformation radius.

The above approximation regards the individual components as nondispersive and thus underestimates the evolution time by 5%–15%. Nevertheless, it provides an excellent representation of the plume's structure and the manner in which it evolves. This is true not only for the QG solution but also for the midlatitude SWE solution (see DPS, Fig. 5).

b. Effect of decreasing latitude

Figure 4 shows five plume snapshots for increasing values of β (decreasing values of reference latitude). At the top of each panel are presented the value of β, the latitude of the boundary θ_0, the deformation radius L_d, and the dimensional time t^* of the snapshot. The spatial dimensions in each panel are normalized by the deformation radius appropriate for that panel. The top panel represents the small β limit ($\beta = 0.005$, $\theta_0 \approx 41°$), which DPS showed to be well approximated by the QG solution. An important point to note is that the small-scale oscillations in the plume amplitude are not present in the QG solution. In the second panel ($\beta = 0.025$, $\theta_0 \approx 19°$), we begin to see the plume-amplitude oscillations. As β is increased (θ_0 decreased) in successive panels, the amplitude of these oscillations increases relative to the plume amplitude.
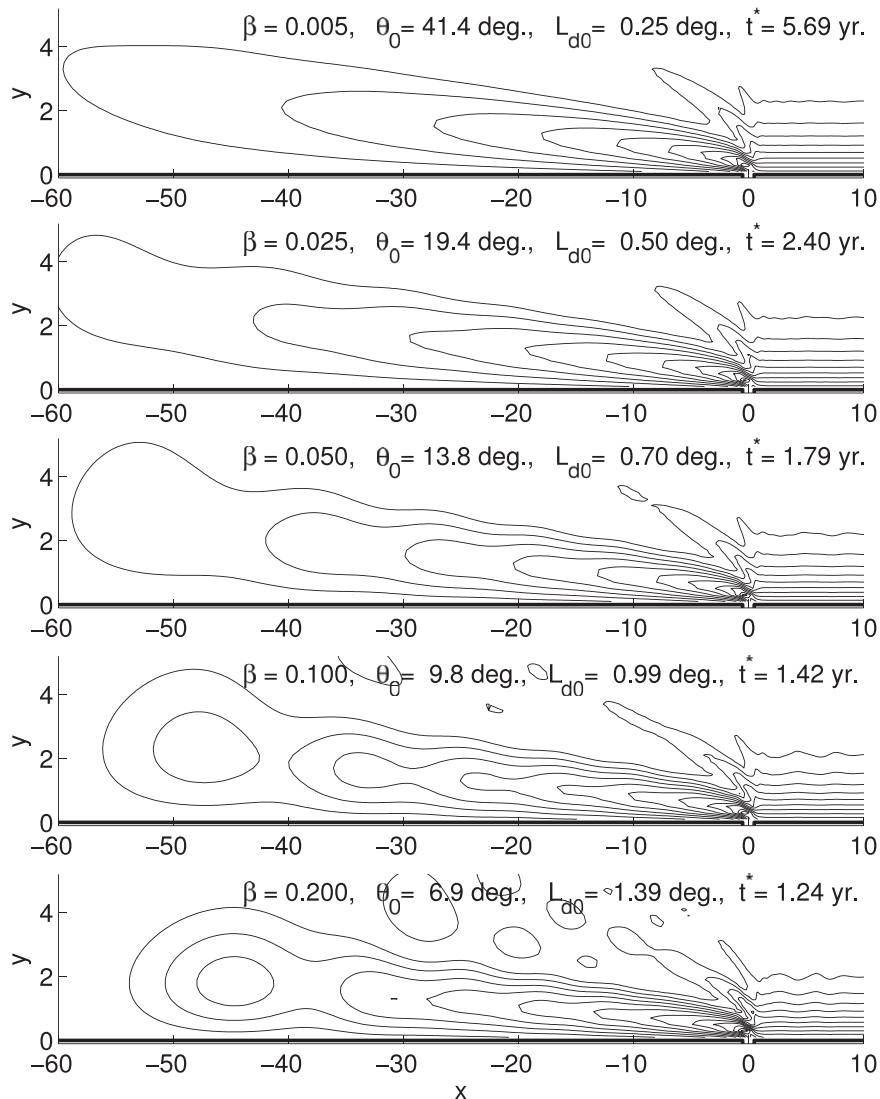
FIG. 4. Effect of increasing β (decreasing latitude) on outflow response in numerical solutions of the linear shallow-water equations. Contours of $\delta h/w\mathrm{Ro}$; contour interval: 0.1.

Figure 5 shows the evolution of the SWE plume at $x = -5.5$ for $\beta = 0.1$, corresponding roughly to the Lombok Strait latitude. In this case, L_d corresponds to about 1° of latitude. The plume profiles are exhibited at approximately the same values of βt as those in Figs. 4 and 5 in DPS, but the times are adjusted slightly to fall midway between extremes of the SWE plume's amplitude oscillations. The SWE solution is represented by the solid line, and the dashed line represents the long-wave approximation, with N chosen in each panel to match the offshore distances of the plumes' peaks. We see that the SWE plume evolution is qualitatively the same as that of the QG plume, and that the long-wave approximation again provides a good estimate of the main peak's structure. For a comparable width of the peak, the long-wave approximation evolves roughly 12% faster and underestimates the amplitude by 5%–8%. The match gets progressively worse farther offshore because of the β effect, but we are not concerned with this small-amplitude, far-offshore response.

c. Differences between the QG and SWE β planes; oscillations in plume amplitude

Although the QG solution provides both qualitative and quantitative insights into the behavior of the mean SWE β plume, it provides no clue as to the origin of the plume-amplitude oscillations. We show in this section that these oscillations are associated with an additional
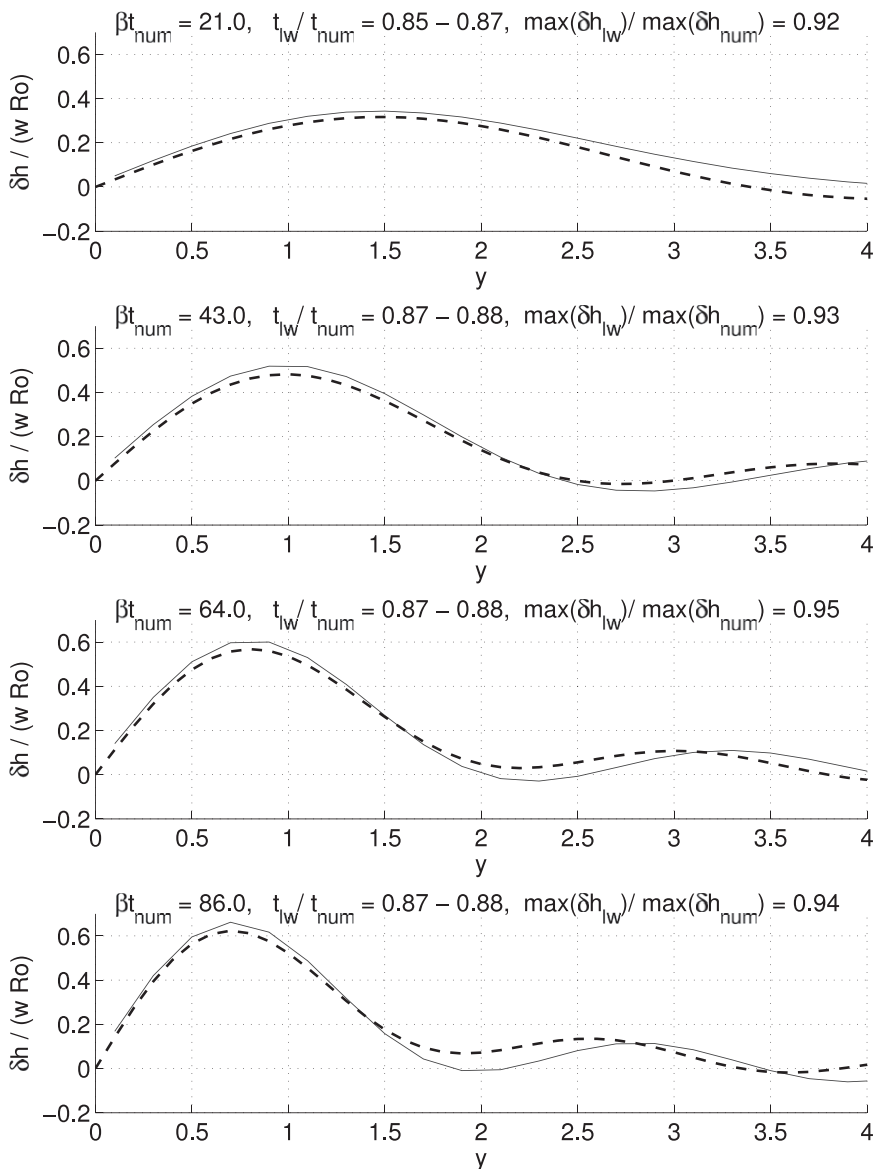
FIG. 5. The β-plume evolution for $\beta = 0.1$ at $x = -5.5$. Solid lines: numerical solutions of the linear shallow-water equations. Dashed lines: long-wave approximation to the linear quasi-geostrophic equation.

near-mouth adjustment process forced by changes in the deformation radius over the offshore extent of the Kelvin current.

In the nondimensional QG representation of DPS, the streamfunction is equal to the model's layer thickness deviation, and it varies across the outflow channel mouth from $\delta h = 0$ at the western corner to $\delta h = w(\text{Ro})$ at the eastern corner. The thickness deviations along the $y = 0$ boundaries to the west and east of the channel are equal to the values at the respective channel mouth corners, and all of the outflow transport is carried eastward by the Kelvin current. On the shallow-water

β plane, the situation is not so simple. If the boundary conditions were to remain as specified in the QG model, the eastward transport in the Kelvin current would be

$$U_K = \int_0^L \frac{(-\partial_y h)}{1 + \beta y}\, dy < \int_0^L (-\partial_y h)\, dy = w\, \text{Ro}. \quad (13)$$

The Kelvin current could no longer carry the entire outflow volume flux because $f = 1 + \beta y$ is larger throughout the interior of the domain than it is at the outflow latitude. The variation of f also allows the β plume to carry a net westward transport if, as in the QG
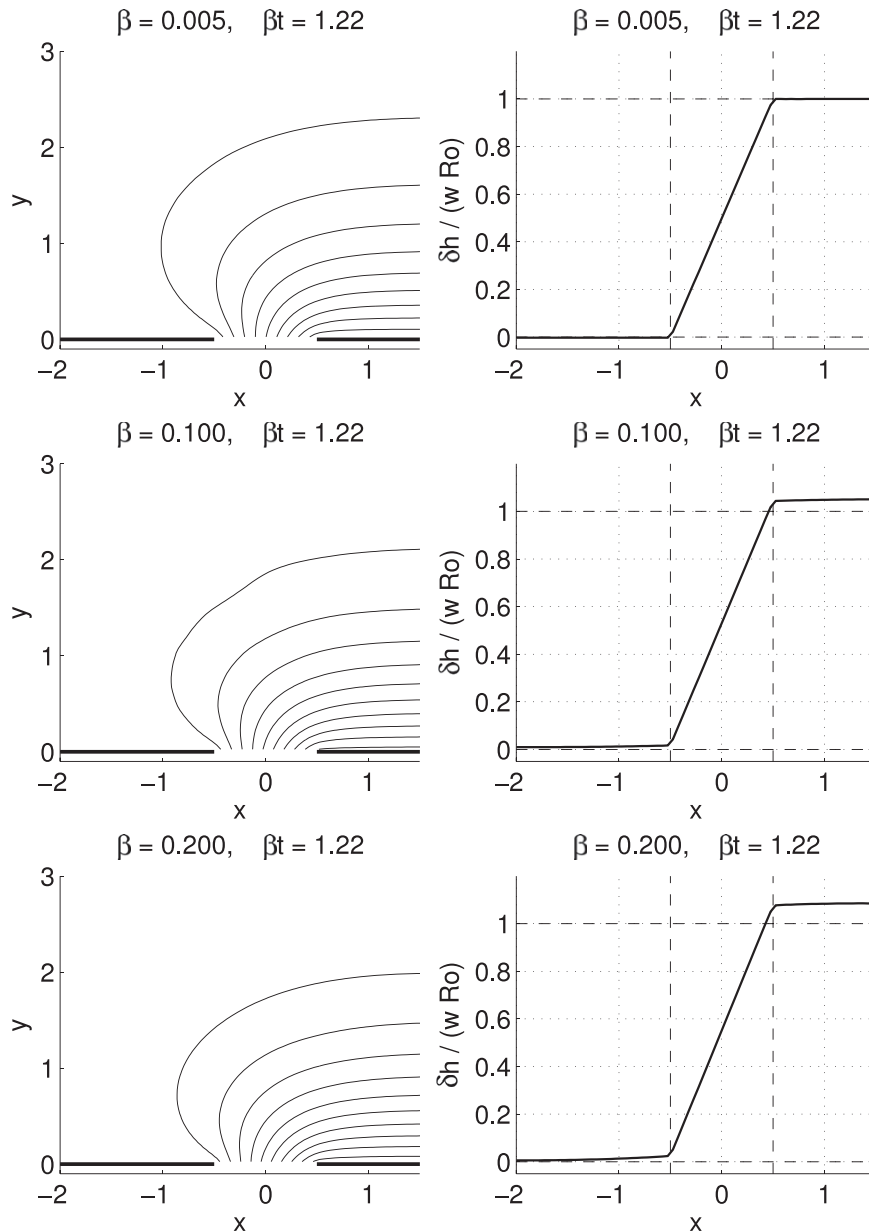
FIG. 6. Kelvin wave boundary pressure on shallow-water β plane. (left) Contours of $\delta h/w\mathrm{Ro}$; (right) $\delta h/w\mathrm{Ro}$ at $y = 0$ in the vicinity of the outflow channel mouth. (top) $\beta = 0.005$ ($\theta_0 = 41.4°$); (middle) $\beta = 0.1$ ($\theta_0 = 9.8°$); (bottom) $\beta = 0.2$ ($\theta_0 = 6.9°$).

model, the thickness deviation vanishes on both boundaries to the west of the channel. With the constraints that we have observed on the β-plume development, however, it is not obvious that the dynamics will provide the necessary transport balance between the Kelvin current and the β plume required for the SWE δh boundary conditions to remain the same as those for the QG model.

The numerical SWE model is forced by a specified outflow at the channel mouth, with no normal flow at other boundary locations, and the layer thickness at the boundary is free to evolve as it will. We examine the impact of β on the short-time boundary values in Fig. 6, where numerical SWE solutions are shown at $\beta t = 1.22$. At this time the Kelvin current is fully developed near the channel mouth, but significant Rossby wave propagation has yet to ensue (cf. top left panel with the $t = 0$ QG solution in Fig. 2 of DPS). The scenario in the top row ($\beta = 0.005$, $\theta_0 \approx 41°$) has been shown to be virtually identical to the QG solution. The middle row ($\beta = 0.1$)

shows solutions for a reference latitude of about 10° (close to that of Lombok Strait) and the bottom row ($\beta = 0.2$) for a reference latitude of 7°. To achieve a good separation between the Kelvin wave and the Rossby waves at the lower latitudes, the initial taper to the outflow velocity had to be decreased, thus increasing the amplitudes of inertia–gravity waves generated by the initial pulse. Evidence of this can be seen in the warping of the lowest-level contour in the middle left panel, but otherwise the Kelvin current representation is unaffected. In the left column, the most noticeable effect of increasing β (lowering latitude) is a "squeezing" of the contours toward the boundary due to a decrease in L_d over the domain, an effect that gets more pronounced with decreasing latitude. A closer inspection, however, also shows that the boundary value of the thickness deviation appears to increase with increasing β.

For each of the three values of β, the right column of Fig. 6 shows the boundary values of the normalized thickness deviation $\delta h/(w\mathrm{Ro})$ in the vicinity of the outflow channel mouth. In the top right panel, $\delta h = 0$ to the west of the channel mouth and $\delta h = (w\mathrm{Ro})$ to the east of the mouth, as in the QG model. The middle and bottom panels, however, show that the boundary values at both corners of the channel mouth have increased and that this effect increases with decreasing latitude. This indicates the presence of a near-mouth process not found in the QG model. Besides having to adjust to the unbalanced βv of the Kelvin wave sweeping around the corner, the model must respond to an additional, rapid increase in layer thickness across the channel mouth, which is apparently caused by the "squeezing" of the Kelvin wave as it rounds the corner. The fact that this effect increases with decreasing latitude suggests a dynamical connection with the plume-amplitude oscillations, which were also seen to increase in amplitude with decreasing latitude (Fig. 4). (We note that the gradient of δh across the channel mouth also appears to increase with decreasing latitude. This is likely an indication of an increasingly negative $\partial_t u$ associated with a more rapid β-plume development at lower latitudes. As the long Rossby wave front propagates away, the value of δh at the western corner rapidly approaches that at the eastern corner, resulting in a uniform δh offset across the channel mouth.)

The rapid increase in interface displacement across the channel mouth (which must also occur within the channel in order to maintain the prescribed outflow) is reminiscent of switched-on Ekman pumping or buoyancy forcing problems (see Cane and Sarachik 1976; Davey and Killworth 1989). The switched-on forcing contains a broad spectrum of frequencies, and the response near the Rossby wave cutoff frequency consists of Rossby waves with zero or near-zero group velocity. In the absence of dissipation, these waves persist indefinitely in the vicinity of the forcing as the long Rossby wave front propagates away.

Figure 7 shows the dimensional periodicity of the plume-amplitude oscillations, measured at $x = -5.5$ and at five different reference latitudes. For near-mouth dynamics, we expect both α, the effective-latitude parameter in (4), and l, the meridional wavenumber, to be $O(1)$. The solid line in Fig. 7 traces the predicted Rossby wave cutoff period as a function of latitude for the values $\alpha = 1.4$ and $l = 0.6$. The plume-amplitude oscillations in the numerical solutions clearly show a strong correlation with the cutoff period. In sum, the evidence strongly indicates that these oscillations are a zero group-velocity response to the β effect's squeezing of the Kelvin wave as it exits the channel mouth and rounds the corner. We note in passing that the increase in boundary pressure is not sufficient to maintain 100% of the outflow volume flux in the Kelvin current. The fractions of the outflow's volume and energy fluxes that are carried by the β plume increase with decreasing latitude.

4. Nonlinear solutions

This section presents numerical solutions to the nonlinear shallow-water problem, and a model for prediction of the plume amplitude as a function of the nondimensional parameter $w\mathrm{Ro}/\beta$. We first show solutions to the weakly nonlinear, inviscid problem (section 4a) that develop stronger oscillations in the plume amplitude than does the linear model but that do not develop robust eddies within the time constraints dictated by numerical stability limits. Nevertheless, these solutions nicely illustrate the concepts of arrested plume evolution and of a critical isobar that separates the near–channel mouth flow into inertial and quasi-linear regimes. Based on these concepts, a mathematical model is developed in section 4b that is shown to be a good predictor of the plume amplitude over a range of outflow velocities and latitudes. In section 4c we show solutions to the strongly nonlinear, viscous problem with no-slip boundary conditions, which develop eddies that are strong enough that a mean plume is no longer visible. By equating the plume amplitude to the mean of the maximum thickness deviation in the eddy field, however, we demonstrate that the plume-amplitude predictor presented in section 4b is still able to predict the amplitudes of the robust eddies. We further show that the periodicity of the robust eddies closely tracks the latitude-dependent zero group-velocity periods of the linear model.
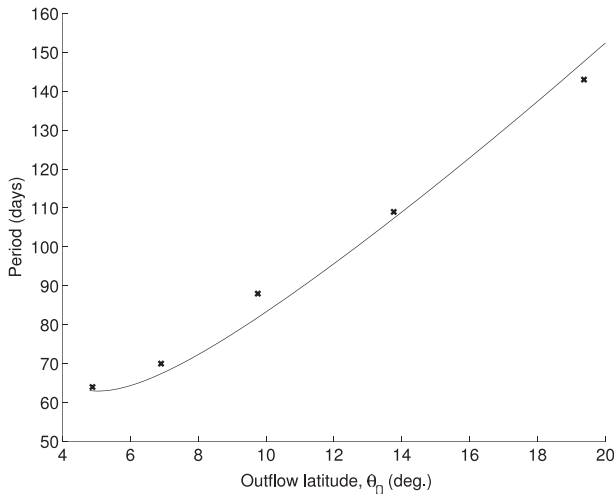
FIG. 7. Latitude dependence of oscillation period in the linear, inviscid model. The solid curve traces the loci of Rossby wave cutoff frequencies (i.e., zero group-velocity frequencies) for $\theta_e = \theta_0 + 1.4L_d$, $l = 0.6$ [see definition of effective latitude (4)].

Illustrative examples in this section will use $\beta = 0.1$, for which $\theta_0 = 9.8°$ and the deformation radius corresponds to $0.99°$ of latitude. Spatial dimensions in the figures will be shown in degrees of latitude and longitude.

a. Inviscid solutions

Without explicit viscosity, the advection scheme in our numerical model is subject to a spurious enstrophy cascade to grid-scale noise over long integrations. Nevertheless, valuable information can be gathered from the inviscid model at integration times that fall far short of the "enstrophy catastrophe." Figure 8 shows 1-yr snapshots of the upper-layer thickness deviation for the nonlinear, inviscid model with various levels of forcing. The reference latitude is close to that of Lombok Strait ($\beta = 0.1$, $\theta_0 = 9.8°$). Plumes are shown for four different values of the outflow Rossby number, corresponding to an outflow velocity range of 0.27 cm s^{-1} (Ro = 0.001) up to 54 cm s^{-1} (Ro = 0.2). The Ro = 0.001 solution is virtually identical to the linear solution (cf. top panel with fourth panel of Fig. 4).

In each panel of Fig. 8, the thickness deviation has been normalized by the corresponding value of wRo so that the plumes are being visualized relative to the maximum thickness deviation in the outflow channel. Contour intervals are wRo/10, and we will refer to the normalized thickness-deviation contours simply as isobars.

We define the relative plume amplitude A_p as the maximum thickness deviation in the meridional profile at a given $x = x_1$ and $t = t_1$, normalized by the maximum outflow thickness deviation:

$$A_p(x_1, t_1) \equiv \frac{\max[\delta h(x_1, y, t_1)]}{w\text{Ro}}. \tag{14}$$

It is important to emphasize at this point that we are discussing a *relative* plume amplitude. In what follows, we will refer to A_p simply as the plume amplitude and we will see that it decreases with increasing outflow transport. In contrast, the unnormalized amplitude of the plume wRoA_p increases with increasing outflow.

In the QG model, the near-mouth value of A_p would be equal to the fraction of the outflow that initially turns west into the β plume (a fraction that evolves with time). In the nonlinear, shallow-water β-plane case, A_p is still proportional to the fractional westward flow, but the proportionality factor is a function of wRo, β, and the offshore distance of the plume's peak because of nonlinearity and the β effect.

The dashed lines in Fig. 8 approximate the plume-amplitude loci between $x^* = -20°$ and $x^* = -2°$. Within this longitude range, an increasing Rossby number is associated with the plume losing its wedge-like shape and becoming more zonal and with the near-mouth locus of the amplitude moving offshore. By counting contours at $x^* = -5°$, we also see that the near-mouth plume amplitude decreases with increasing Rossby number.

The above observations suggest that the plume evolution seen in the linear model is being arrested in the nonlinear model, with the arrest occurring earlier in the evolutionary process for stronger outflows. In Fig. 9, we show that this does appear to be the case. Plume profiles at $x^* = -6°$ are shown in three panels corresponding to Ro = 0.001, 0.05, and 0.2. In each panel, snapshots of the profiles are shown at six successively longer times, which are the same for each panel: $t^* = 57, 77, 134, 258, 335$, and 366 days. The small-scale oscillations in plume amplitude at Ro = 0.05 are approximately 15% of A_p, and the last two time intervals were chosen to filter out these oscillations. In each panel, the initial profile at $t = 57$ days is represented by a heavy solid line, and the final profile at $t = 366$ days is represented by a heavy dashed line. At intermediate times, the profiles evolve toward a higher peak, closer to the equatorward boundary. The quantitative match between panels is not perfect, in part because of a phase difference between the plume-amplitude oscillations at different values of Ro, but the pattern is clear. At 57 and 77 days, the profiles at all three forcing levels look very similar, and as time progresses the profiles evolve similarly to the linear plume, up to a point. The Ro = 0.2 profile ceases to change significantly shortly after 77 days, and the Ro = 0.05 profile ceases to do so shortly after 134 days. At 366 days, the Ro = 0.001 profile appears to be evolving still, as in the linear model.
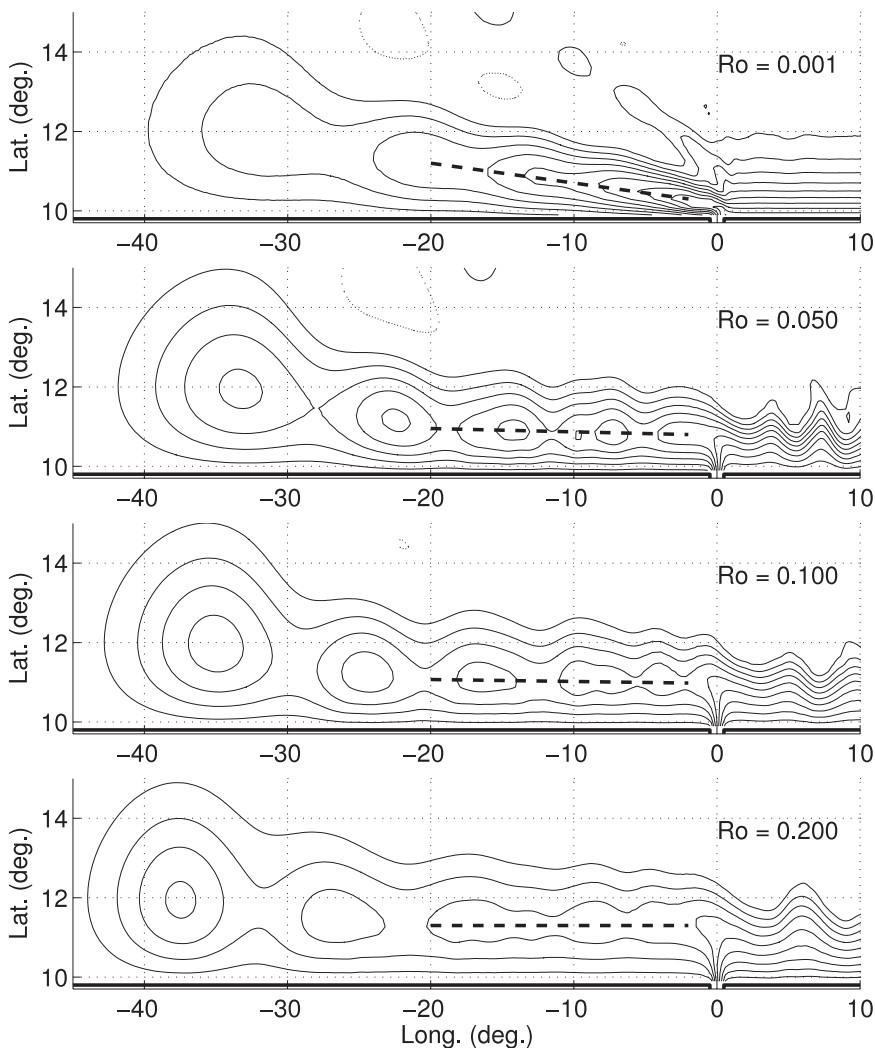
FIG. 8. Effect of increasing outflow on inviscid model; β plumes associated with nonlinear outflows at $t^* = 1$ yr for $\beta = 0.1$, $w = 1$. Contours of $\delta h / w \mathrm{Ro}$ from numerical solutions; contour interval: 0.1. Dashed lines approximate the loci of maximum δh within the plumes on $-20° < x^* < -2°$.

For a different perspective, Fig. 10 shows a time series of snapshots of the isobars in the vicinity of the channel mouth for Ro = 0.001, 0.05, and 0.2. The snapshots are taken at 21, 52, 142, and 250 days. At all three forcing levels, the flow at 21 days exhibits the initial Kelvin wave structure. The isobars balloon out from the channel mouth to form a Kelvin-like cross-current decay, so that the near-mouth meridional velocities are stronger to the east and weaker to the west. The isobars then bend eastward into the Kelvin current proper. As the Rossby adjustment proceeds, the isobars begin to bend more to the west as they exit the channel mouth, starting with the most westward isobar and proceeding with each successive isobar to the east as time progresses. In the essentially linear case, this process continues until all

of the isobars bend to the west upon leaving the channel mouth. In each of the stronger forcing cases, however, a critical isobar can be identified which separates a region of Rossby wave shedding to the west from a region to the east where the flow is in a quasi steady state. In the channel mouth vicinity east of the critical isobar an inertial balance dominates, with time dependence playing a negligible role. As the outflow velocity increases, a larger fraction of the outflow is able to achieve this inertial balance and the critical isobar migrates westward across the channel mouth. Accordingly, more of the outflow goes directly into the Kelvin current at all times. West of the critical isobar, where the velocities are weaker, the westward Rossby wave propagation proceeds in a manner similar to the linear model.
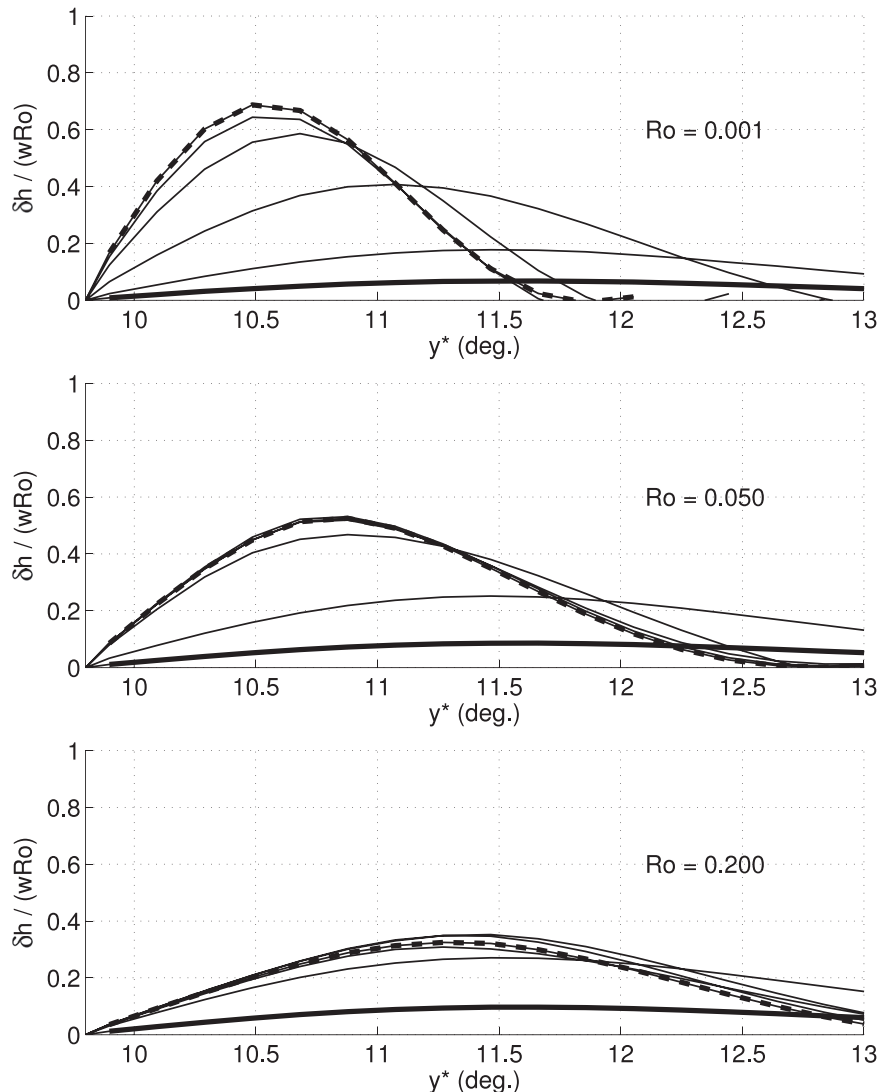
FIG. 9. Arrested plume evolution. Snapshots of meridional plume profiles at $x^* = -6°$, $t^* = 57$, 77, 134, 258, 335, and 366 days. Here $\beta = 0.1$; (top) Ro = 0.001, (middle) 0.05, and (bottom) 0.2.

The thickness deviations in Fig. 10 were contoured at wRo/10 intervals, and the thick contour in each panel was chosen to represent the critical isobar within the accuracy of the contour spacing. For Ro = 0.05, the displayed critical isobar is $\delta h_c = 0.6\,w$Ro, and, for Ro = 0.2, $\delta h_c = 0.4\,w$Ro. Between these two scenarios the outflow velocity (Ro) was increased by a factor of 4, but the value of the normalized critical isobar $\delta h_c/w$Ro decreased only by a factor of 2/3. Consequently, while the fraction of the outflow available to feed the β plume decreases as the outflow is increased, the actual volume flux into the plume nevertheless increases.

The similarity between the plume profiles in Fig. 9 and the early stages of the linear plume, together with the identification of the relative plume amplitude A_p with $\delta h_c/w$Ro as evidenced in Fig. 10, suggests an exploitable connection between the critical isobar concept and the plume-evolution model. We propose that the arrested plume evolution apparent in Fig. 9 arises from the ability of the strong velocity field near the critical isobar to arrest the propagation of the slower, higher meridional-mode Rossby waves. The effect on the wave propagation speed will be a combination of Doppler shift and modification of the mean potential vorticity gradient by the near-mouth flow field. While a precise analysis of this effect is beyond the scope of our study, we can reasonably expect that progressively stronger, quasi-steady eastward velocities in the neighborhood of the channel mouth will be capable of arresting the westward propagation of progressively lower meridional-mode
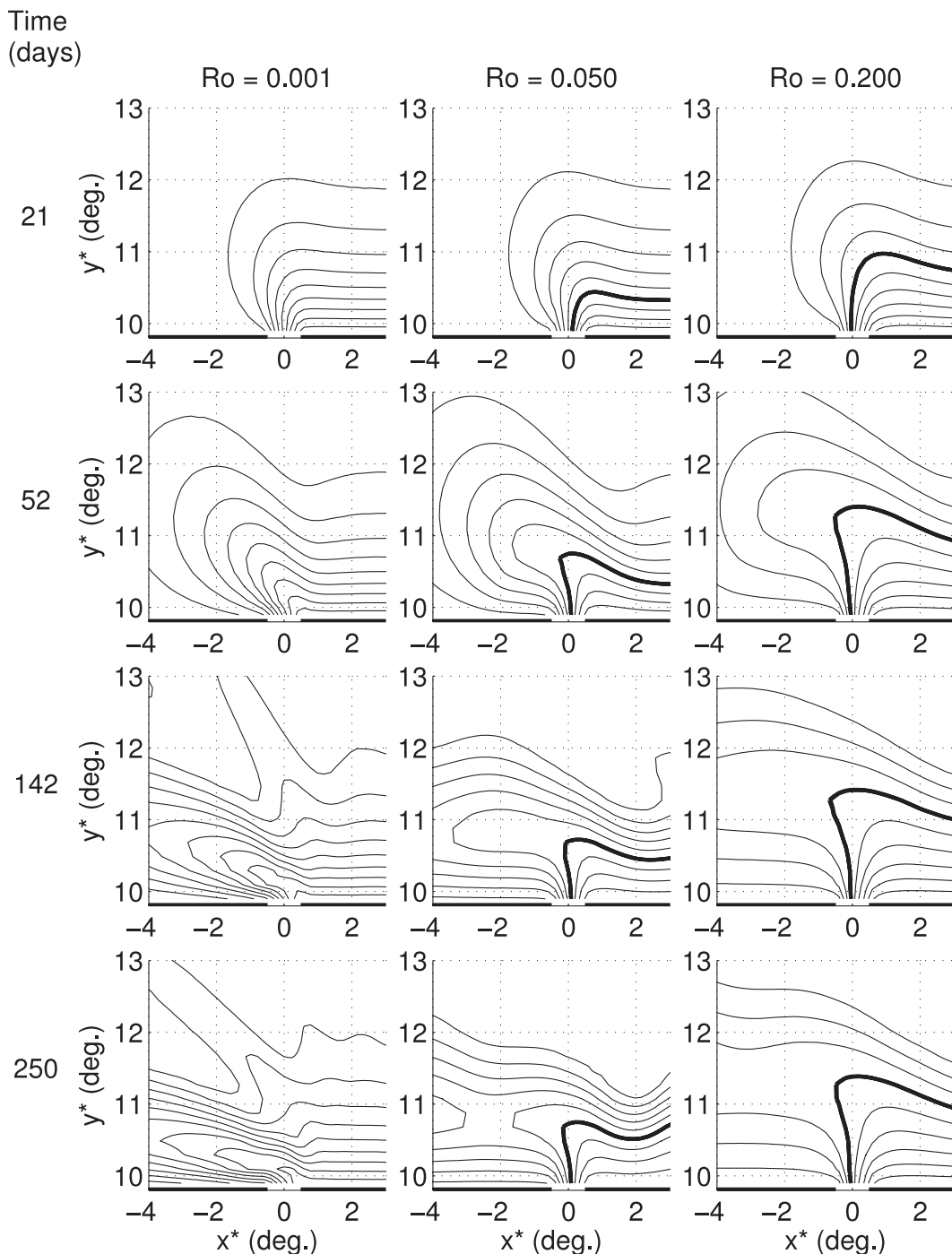
FIG. 10. Critical isobar concept, contours of $\delta h/w\text{Ro}$. Contour interval: 0.1; $\beta = 0.1$; $w = 1$. Each column contains solutions for the value of Ro at the top of the column. Each row contains solutions for the time (days) at the left of the row. Critical isobar (δh_c) represented by thick contour. For Ro = 0.05, $\delta h_c/w\text{Ro} = 0.6$. For Ro = 0.2, $\delta h_c/w\text{Ro} = 0.4$.

Rossby waves, thus arresting the plume at progressively earlier stages in the evolutionary process.

For conceptual simplicity, we identify a near-mouth critical zonal velocity u_c that is proportional to the strength of the near-mouth zonal velocity field and capable of arresting the westward propagation of any Rossby wave whose magnitude of unmodified westward propagation speed is less than u_c. We have only to reassure

ourselves of an expected positive correlation between the strength of the near-mouth zonal velocity field and the magnitude of the critical isobar δh_c.

Figure 11 shows contours of $u/\delta h_c$ at four different times for Ro = 0.05 and Ro = 0.2. The value of δh_c for each scenario was given above. The times were chosen to span the interval from just before the Ro = 0.2 plume stops evolving to just after the Ro = 0.05 plume stops evolving (see Fig. 9). Only the contours for $u > 0$ have been displayed, the contour interval is 0.1, and the thick contour represents $u/\delta h_c = 0.8$. For reference, the critical isobar is delineated by a medium-thick curve and the $x = 0$ transect by a dashed line. When Ro = 0.05, the maximum value of $u/\delta h_c$ at $x = 0$ stabilizes in the range 0.9–1.0, and when Ro = 0.2, the corresponding maximum value of $u/\delta h_c$ stabilizes in the range 0.7–0.8. These numbers are only ballpark estimates because δh_c was chosen in each case only to within the accuracy of the $w\text{Ro}/10$ contours. The important points of the figure, however, are that there does appear to be a near-stationary u field in the vicinity of the channel mouth that retains a similarity of structure over a wide range of Ro, that the zonal velocities decrease rapidly to the west of the channel mouth, and that the maximum near-mouth u is proportional to δh_c (although the proportionality factor may have a weak dependence on Ro). The evidence supports the reasonableness of our proposed critical velocity concept as well as the expected positive correlation between δh_c and u_c, which we will use in the next section to develop a quantitative model of the arrested plume.

b. Arrested plume model

We have seen that the long-wave approximation to the linear QG model produces a calculable description of the linear plume evolution that is reasonably accurate even on the shallow-water β plane. Accordingly, and given the above observations of Figs. 8–11, we propose a simplistic mechanism for the plume generation in a hybrid linear–nonlinear QG model, where the linear behavior is described by the long-wave approximation:

1) Increasing the outflow volume flux allows the faster, easternmost part of the near-mouth flow field to achieve a dominantly inertial balance, that is, $\beta \, \partial_x \psi \sim J \, (\psi, \nabla^2 \psi)$. This region is separated by a critical streamline, ψ_c, from the region to the west where the dominant balance is $\beta \, \partial_x \psi \sim (\nabla^2 - 1) \partial_t \psi$. This latter region continues to shed Rossby waves in a process similar to that seen in the linear model.

2) The critical streamline is associated with and proportional to a critical zonal velocity that is capable of arresting westward Rossby wave propagation in the vicinity of the channel mouth:

$$u_c = \gamma \psi_c. \quad (15)$$

The proportionality factor may have a weak inverse relationship with Ro (Fig. 11) but, as a first approximation, we treat it as a constant that is yet to be determined.

3) The critical zonal velocity arrests the propagation of Rossby waves that have a westward propagation speed smaller than u_c. The highest meridional mode to escape the channel mouth vicinity has mode number N_c, where

$$u_c - \frac{\beta}{l_{N_c+1}^2 + 1} = 0. \quad (16)$$

4) Once meridional mode N_c has reached a given $x = x_1$, the plume evolution at that point is then arrested for all time, with a meridional structure given by the long-wave approximation (11) truncated at N_c:

$$\psi(x_1, y) = w\text{Ro}\frac{2}{L}\sum_{n=1}^{N_c}\frac{l_n}{l_n^2 + 1}\sin l_n y, \quad (17)$$

with $l_n = n\pi/L$.

5) On $x_1 < x < 0$ the plume assumes a purely zonal structure, and continuity of the streamfunction requires that the value of the streamfunction at the peak of $\psi(x_1, y)$ equal the value on the critical streamline:

$$\psi_c = \max[\psi(x_1, y)]. \quad (18)$$

6) With the relative plume amplitude A_p as defined in (14), equating the streamfunction with the δh as previously discussed and using (15)–(18), we have

$$A_p = \frac{\psi_c}{w\text{Ro}} = \max\left(\frac{2}{L}\sum_{n=1}^{N_c}\frac{l_n}{l_n^2 + 1}\sin l_n y\right). \quad (19)$$

7) Combining (15), (16), and (19), we also have

$$\frac{w\text{Ro}}{\beta} = [\gamma(l_{N_c+1}^2 + 1)A_p]^{-1}. \quad (20)$$

We have observed that the evolution of A_p is monotonic, so there is a one-to-one relation between A_p and N_c, with A_p increasing as N_c does. Consequently, (20) shows that there is also a one-to-one relation between $w\text{Ro}/\beta$ and N_c. By stepping through a sequence of N_c
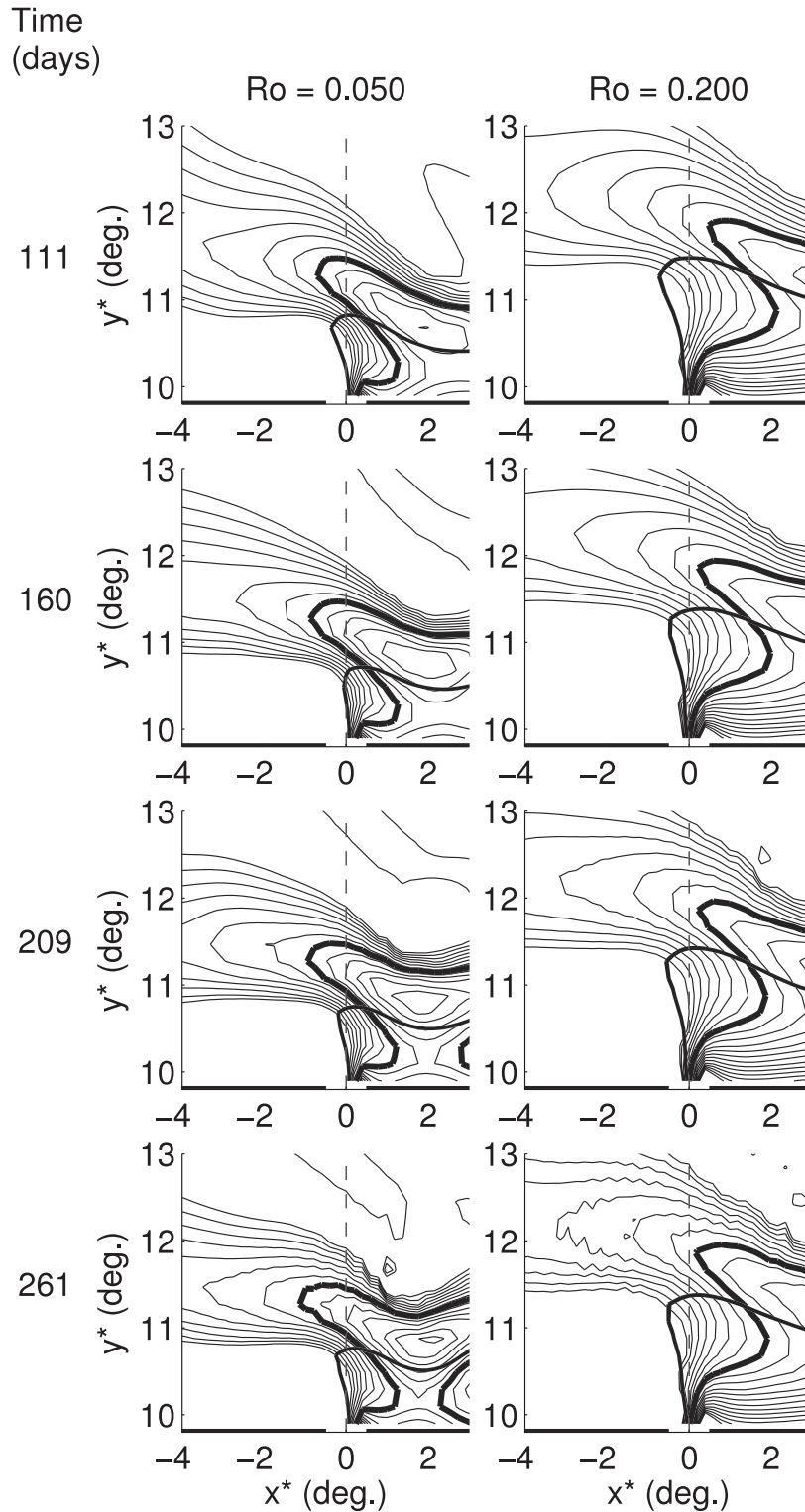
FIG. 11. Dependence of near-mouth zonal velocity on the value of δh_c. Contours of $u/\delta h_c$ for $\beta = 0.1$, $w = 1$. For Ro = 0.05, $\delta h_c/w$Ro = 0.6. For Ro = 0.2, $\delta h_c/w$Ro = 0.4. Contours shown for $u > 0$ only; contour interval: 0.1. Thick contours represent $u/\delta h_c = 0.8$. Medium-thick contour that crosses u contours represents the critical isobar δh_c (as in Fig. 10).
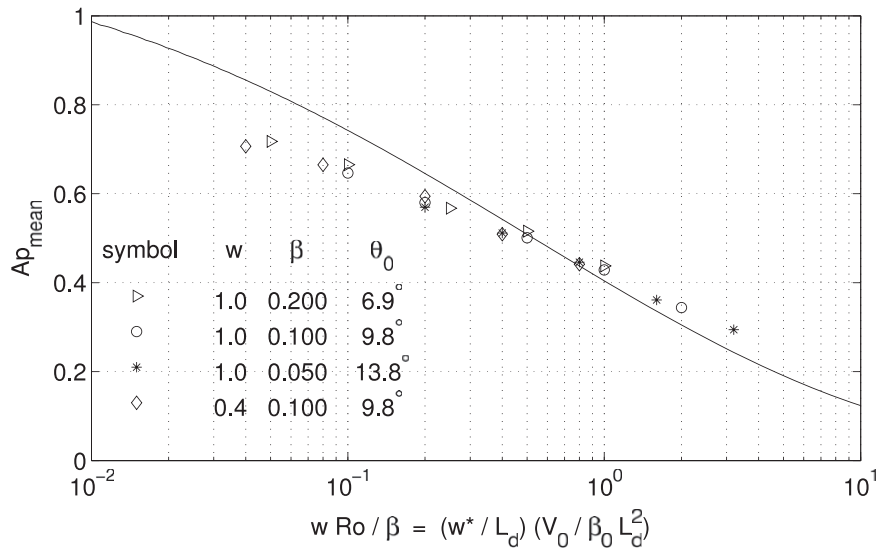
FIG. 12. Numerical solutions for the mean plume amplitude (Ap_{mean}) in the nonlinear, inviscid shallow-water equations. Individual symbols: solutions for Ap_{mean} vs $w\mathrm{Ro}/\beta$ for $w = 1.0$, $\beta = 0.05$, 0.1, and 0.2; and for $w = 0.4$, $\beta = 0.1$. At each combination of w and β, solutions were obtained for five different values of Ro. Solid curve represents the plume prediction solution obtained from (19) and (20) with $\gamma = 0.5$.

values, we can numerically determine the relation between A_p and $w\mathrm{Ro}/\beta$ for a given value of γ. Note that Ro/β is the ratio of the outflow velocity to the westward propagation speed of the $(k, l) = (0, 0)$ Rossby wave. Because of the complexity of the near-mouth velocity field (Fig. 11), we do not have an a priori estimate for γ other than we expect it to be $O(1)$. At this point we regard it as a fitting parameter by which we can test the utility of our proposed mechanism.

Figure 12 shows discrete values of the time-mean plume amplitude Ap_{mean}, plotted versus $w\mathrm{Ro}/\beta$, from numerical solutions of the inviscid SWE in which $w = 1$ and $\beta = 0.05, 0.1, 0.2$, while Ro ranges between 0.01 and 0.2. Also shown are calculations for $w = 0.4$, $\beta = 0.1$ over the same range of outflow velocities. The solid line is the plume-amplitude prediction curve derived from (19) and (20), using the value $\gamma = 0.5$. The solutions cluster well in their dependence on $w\mathrm{Ro}/\beta$, and the match with the prediction curve is reasonably good. The difference in slope between the curve and the numerical solutions is consistent with γ having an inverse relationship with $w\mathrm{Ro}/\beta$, which in turn is consistent with our observations of Fig. 11. Without a deeper understanding of the Rossby wave-arresting process, however, further refinements in the estimate of γ are not justified nor are they necessary. The given curve provides a particularly good estimate of A_p for $w\mathrm{Ro}/\beta > 0.5$, in which range we will find the strong eddy generation that we seek.

c. Viscous solutions

We now consider numerical solutions of the viscous model, which allow us to explore the effect of stronger outflows. To compare solutions at a variety of forcing levels without overdamping the low Rossby number solutions, we keep the Reynolds number (6) constant at $\mathrm{Re} = 1000$. No-slip boundary conditions are applied as the most realistic choice for a near-boundary viscous flow.

Figure 13 shows a series of 1-yr snapshots of the $\delta h/w\mathrm{Ro}$ field for $\beta = 0.1$, $\mathrm{Ro} = 0.1, 0.2, 0.3$, and 0.4. The $\mathrm{Ro} = 0.1$ case (top panel) is quite similar to the corresponding inviscid case (third panel of Fig. 8) with only slightly more plume variability near the outflow mouth. In the other panels, however, robust eddies are visible to the extent that a mean plume is no longer visible over a range of longitudes. This range gets larger in successively lower panels, indicating that the time between the initiation of the outflow and the generation of strong eddies decreases as the outflow increases. Note also that the distance between eddies increases only gradually with increasing outflow. This "eddy wavelength" evolves from the wavelength of the plume-amplitude oscillations seen in the top panel, which, as we saw in Fig. 8, evolve gradually from the plume-amplitude oscillations of the linear model.

In the presence of a strong eddy field, we extend our definition of the plume amplitude A_p to the regions between eddies where there may be no local maximum
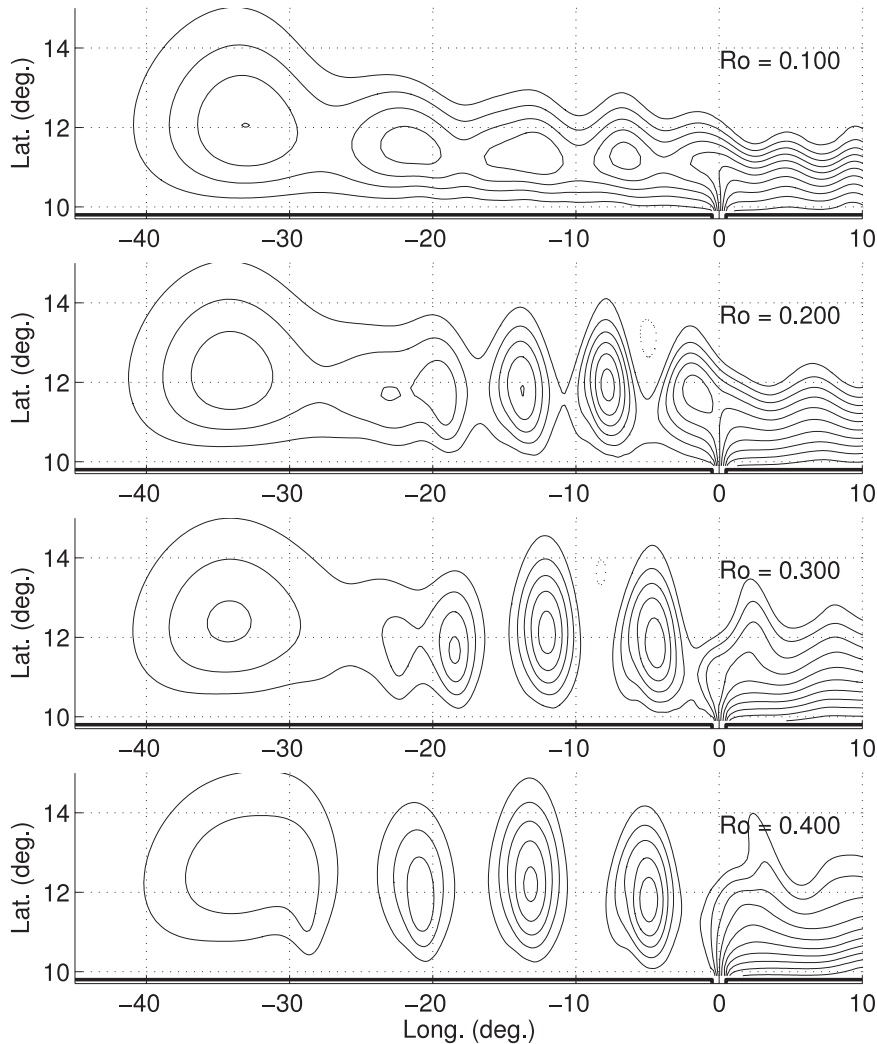
FIG. 13. Effect of increasing outflow on viscous, no-slip model. Snapshots after one year for $\beta = 0.1$, Re = 1000.

in the meridional profile of δh. In this case, we define A_p to be the value of $\delta h/(w\text{Ro})$ tracked most directly between the locations where there are clear meridional maxima (i.e., within the eddies themselves). As such, A_p can be zero or even negative between the eddies. Then Ap_{mean} and Ap_{sd} are the mean and standard deviation in a time series of A_p thus constructed. The span of the time series analyzed includes only that period during which the oscillations in A_p appear to have reached a steady state.

The top panel of Fig. 14, in the same format as Fig. 12, summarizes a suite of experiments with the viscous model. Values of β used were 0.05, 0.1, 0.2, and 0.4, corresponding to outflow latitudes of about 14°, 10°, 7°, and 5°. Rossby numbers ranged from 0.01 to 0.6, and the Reynolds number was held constant at 1000. The solid curve represents the same prediction of the A_p versus

$w\text{Ro}/\beta$ relation that is shown in Fig. 12, with $\gamma = 0.5$. Although there is increased scatter in the numerical solutions in Fig. 14, the agreement with the prediction curve over a wide range of latitudes and outflow strengths is still quite good.

The bottom panel of Fig. 14 shows the ratio of the standard deviation of A_p to the mean of A_p, plotted versus $w\text{Ro}$. Solid lines connect the individual measurements corresponding to the same value of β. The dashed line is at $Ap_{\text{sd}}/Ap_{\text{mean}} = \sqrt{2}/2$, which is the standard deviation-to-amplitude ratio of a sine wave. Generally, for each value of β, the relative oscillation amplitude increases rapidly from the near-linear level at $w\text{Ro} = 0.01$ up to a maximum near $w\text{Ro} = 0.2$, after which it asymptotes in the vicinity of $Ap_{\text{sd}}/Ap_{\text{mean}} = \sqrt{2}/2$. Measurements that asymptote exactly on the dashed line for a field of eddies with uniform amplitude
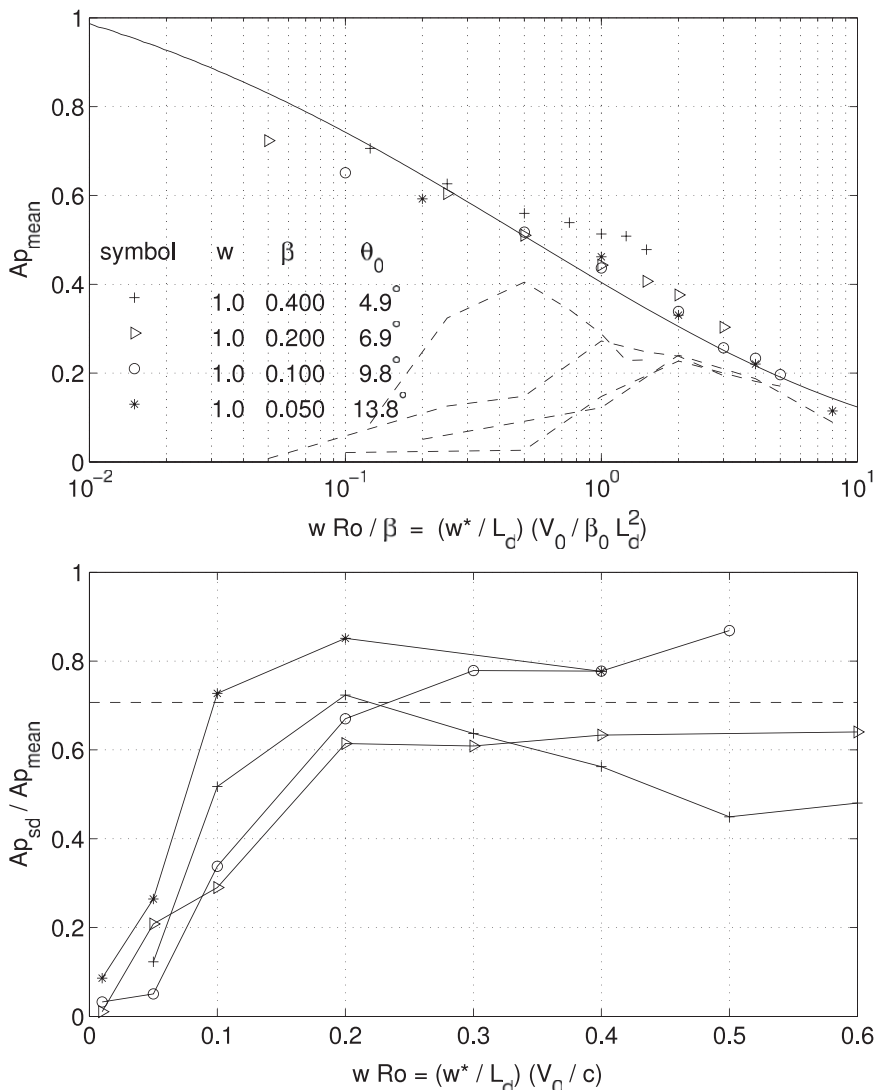
FIG. 14. Numerical solutions for the mean and standard deviation of the plume amplitude (Ap_{mean} and Ap_{sd}) in the nonlinear, viscous SWE with no-slip boundary conditions. (top) Shown is Ap_{mean} vs $w\text{Ro}/\beta$. Solid curve represents the plume prediction solution shown in Fig. 12. Dashed curves represent Ap_{sd} for the various values of β. (bottom) Shown is Ap_{sd}/Ap_{mean} vs $w\text{Ro}$, with symbols as in (top). Each solid curve connects individual solutions for one value of β. The dashed line is at $Ap_{sd}/Ap_{mean} = 2^{-1/2}$.

and spacing would indicate purely sinusoidal variations in A_p, in which the oscillation amplitude is equal to the mean amplitude; that is, A_p varies from zero to twice Ap_{mean} like $(1 + \cos\omega t)Ap_{mean}$. Within the parameter range we have investigated, the oscillations in A_p do appear to approximate this simplistic picture, a view that is supported by the sinusoid-like time series in the bottom panel of Fig. 3 and the regularity of the eddy chains in Fig. 13. Because eddy amplitude typically refers to an isotherm or surface elevation deviation from the ambient, A_p then approximates the half-amplitude of a robust eddy field.

The mean value of A_p in the presence of strong eddies continues to be well predicted by the arrested plume-evolution model, indicating that the near-mouth processes described in the model development continue to operate in the strong eddy-generation regime. Here A_p is a measure of the fraction of the outflow that enters the plume, and that is controlled by the fraction of the outflow that can attain a near-inertial balance in the vicinity of the channel mouth, thus allowing it to enter directly into the eastward-flowing Kelvin current. The volume flux available for nearshore westward transport (to the west of the outflow) is thus fixed by the near-mouth
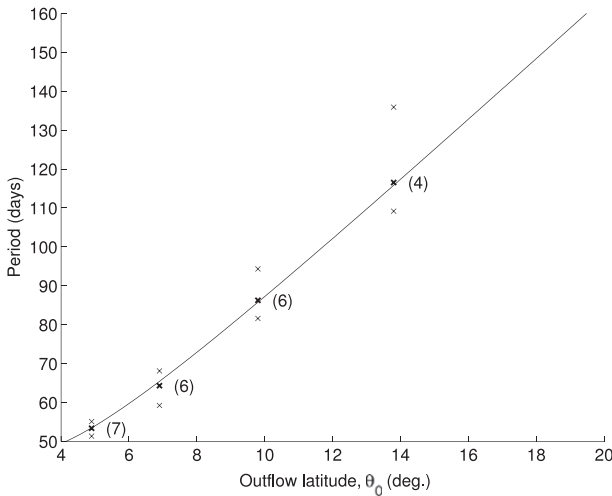
FIG. 15. Latitude dependence of oscillation period in the nonlinear, viscous, no-slip model. The periods are from the various solutions represented in Fig. 14, less the Ro = 0.01 case for each value of β. Heavy x's show averages over the number (shown in parentheses) of different values of Ro. Light x's show the minimum and maximum value of the period within the represented range of Ro. The solid curve traces the loci of Rossby wave cutoff frequencies (i.e., zero group-velocity frequencies) for $\theta_e = \theta_0 + 0.9L_d$, $l = 0.9$ [see definition of effective latitude (4)].

processes, whether that westward transport is carried by a nearly steady β plume or by a strong eddy field.

The dashed lines in the top panel of Fig. 14 are the traces of the Ap_{sd} solutions represented in the bottom panel, but plotted versus $w\mathrm{Ro}/\beta$, with a separate curve for each value of β. The parameter range over which strong eddy motion is expected can thus be seen relative to the A_p prediction curve. With the possible exception of the near-equatorial solutions ($\theta_0 = 4.9°$), the prediction curve matches the numerical solutions reasonably well in this range.

It is worth stating again that A_p represents the plume amplitude (or roughly half the eddy amplitude) normalized by $w\mathrm{Ro}$. While A_p decreases with increasing outflow at a given latitude, the actual plume amplitude and/or eddy half-amplitude $w\mathrm{Ro}A_p$ increases with increasing outflow.

Figure 15 shows the latitude dependence of the eddy period in the viscous model in a format similar to that in Fig. 7. The oscillation periods typically lengthen gradually with increasing outflow, and the bold x's show averages over the number of different values of Ro utilized. The light x's show the minimum and maximum value of the period within the represented range of Ro. The correlation with the near-zero group-velocity Rossby wave period is once again evident. The solid curve traces the loci of the zero group-velocity frequencies for $\theta_e = \theta_0 + 0.9L_d$, $l = 0.9$.

5. Summary and discussion

We have shown that the near-mouth response to a nonlinear poleward outflow on the β plane can be regarded conceptually as consisting of two distinct regimes separated by a critical isobar. A purely inertial regime to the east of the critical isobar flows directly into an eastward Kelvin current, while a quasi-linear regime to the west generates a β plume. As in the linear model, the β plume can be regarded as the dispersive westward propagation of the individual components of the Kelvin current's meridional spectrum. As such, the meridional cross section of the plume at a given longitude evolves, with the amplitude of the plume growing and the peak shifting toward the boundary as time progresses. The evolution is arrested when the slower, higher meridional-mode Rossby waves are not able to escape a critical zonal velocity in the vicinity of the channel mouth. This critical zonal velocity is proportional to the thickness deviation associated with the critical isobar. The proportionality factor is nearly constant over a wide range of outflow strengths, and in our nondimensionalization scheme its value is roughly 1/2. Once the evolution is arrested, the β plume emanating from the vicinity of the outflow becomes a purely zonal shear flow with a constant maximum pressure, which, in the first approximation, is equal to the critical isobar pressure.

When mated with the long-wave approximation's quantitative description of the linear plume evolution, the model described above provides a means for calculating the arrested plume amplitude for a wide range of outflow latitudes and volume transports. When the outflow generates robust eddies that obscure the presence of a β plume, the time mean of the eddy amplitudes is nevertheless well predicted by the plume-prediction model. Within the parameter range we have examined, the time variation of the layer thickness, reflecting the passage of the eddies, is very nearly sinusoidal. The individual eddy amplitudes can therefore be inferred from the mean plume prediction model. The periodicity of the eddies remains close to that of the latitude-dependent, zero group-velocity oscillations observed in the linear model.

Further investigations are beyond the scope of this study, but one obvious issue deserves some speculative comments. That is the question of the actual generation mechanism for the strong eddies. The reader may have noticed that, over 1 yr of integration with $\beta = 0.1$ and Ro = 0.2, the inviscid model produces a plume with little variability (bottom panel, Fig. 8), whereas the viscous model produces robust eddies (second panel, Fig. 13). In the viscous model with free-slip boundary

conditions (not shown) the picture is little different from the inviscid case, so the no-slip boundary condition is clearly responsible for the strong eddies. This is not merely a case of vorticity diffusion through the boundary, however, because cyclonic relative vorticity is being fluxed through the boundary, while the eddies are anticyclonic. Rather, this appears to argue for barotropic instability of the mean plume shear flow. In the inviscid, long-wave approximation of the arrested plume (a purely zonal shear flow), the maximum westward velocity occurs at the boundary, the relative vorticity vanishes at the boundary, and the meridional gradient of relative vorticity has its most negative value at the boundary. The relative vorticity gradient ($-\partial_{yy}u$) changes sign near the peak of the plume where the zonal velocity changes sign, so any change in the sign of the meridional potential vorticity gradient is most likely to occur between the boundary and the plume's peak. As the outflow is increased and the plume is arrested in a "flatter" profile, with the peak further offshore, the value of $-\partial_{yy}u$ at the boundary becomes less negative and a change in sign of the potential vorticity gradient becomes less likely. We thus have the interesting result that the mean plume changes from an unstable to a stable configuration with increasing amplitude ($w\text{Ro}A_p$). This description is consistent with the apparent decrease in plume variability seen in the inviscid model as the Rossby number is increased from 0.05 (second panel, Fig. 8) to 0.2 (bottom panel, Fig. 8).

If the Reynolds number is kept high enough in the viscous model, we expect the viscosity to have little effect on the offshore structure of the plume over short integrations. The free-slip boundary condition, with zero relative vorticity at the boundary, is the viscous scenario most likely to preserve the plume structure of the inviscid model, as described in the previous paragraph. Hence the similarity noted above between the free-slip and inviscid models. By imposing the no-slip boundary condition, however, we automatically increase $\partial_{yy}u$ between the boundary and the plume's peak, thus extending the necessary condition for barotropic instability into a stronger flow regime.

In contrast to the above argument, we recall that the eddies appear to represent an oscillation about the mean plume amplitude, with an oscillation amplitude that is equal to the mean plume amplitude. This implies that the time-averaged energy density in the eddy field is considerably greater than the energy density in an equivalent mean plume, suggesting that the mean plume cannot be the sole energy source for the eddies. In addition, the fact that the onset of strong eddy generation depends on $w\text{Ro}$ (bottom of Fig. 14) rather than on the plume-structure-controlling parameter $w\text{Ro}/\beta$ (top of

Fig. 14) hints at the importance of a near-mouth adjustment process, likely occurring in the transitional region between the inertial and quasi-linear regions, which was not included in the simplified arrested-plume model. We suggest that both shear-flow instability and a near-mouth adjustment process play important roles in the eddy generation.

In addition to the specific nature of the instability process, much remains to be understood about the general outflow behavior. We noted trends in mass flux and energy flux partitioning in the linear model, but these remain to be quantified in both the linear and nonlinear models. In the nonlinear model, the partitioning between radiated and advected energy flux is a matter of interest. The relation between the zero group-velocity waves of the linear model and the oscillations in the strongly nonlinear model calls for a more rigorous dynamical explanation. A complete theory of the outflow in this model will encompass all of the above concerns.

In closing, we note that the 1½-layer poleward outflow model with nonvanishing upper-layer thickness provides valuable insights into the origin of oceanic variability in the IAB that can be extended to other latitudes and outflow conditions. In addition, the model demonstrates a richness of behavior that provides fertile ground for further research.

REFERENCES

Bray, N. A., S. E. Wijffels, J. C. Chong, M. Fieux, S. Hautala, G. Meyers, and W. M. L. Morawitz, 1997: Characteristics of the Indo-Pacific throughflow in the eastern Indian Ocean. *Geophys. Res. Lett.,* **24,** 2569–2572.

Cane, M. A., and E. S. Sarachik, 1976: Forced baroclinic ocean motions. I: The linear equatorial unbounded case. *J. Mar. Res.,* **34,** 629–665.

Chong, J. C., J. Sprintall, S. Hautala, W. L. Morawitz, N. A. Bray, and W. Pandoe, 2000: Shallow throughflow variability in the outflow straits of Indonesia. *Geophys. Res. Lett.,* **27,** 125–128.

Davey, M. K., and P. D. Killworth, 1989: Flows produced by discrete sources of buoyancy. *J. Phys. Oceanogr.,* **19,** 1279–1290.

Durland, T. S., J. Pedlosky, and M. A. Spall, 2009: Response to a steady poleward outflow. Part I: The linear, quasigeostrophic problem. *J. Phys. Oceanogr.,* **39,** 1541–1550.

Feng, M., and S. Wijffels, 2002: Intraseasonal variability in the South Equatorial Current of the east Indian Ocean. *J. Phys. Oceanogr.,* **32,** 265–277.

Nof, D., 2005: The momentum imbalance paradox revisited. *J. Phys. Oceanogr.,* **35,** 1928–1939.

——, T. Pichevin, and J. Sprintall, 2002: ''Teddies'' and the origin of the Leeuwin Current. *J. Phys. Oceanogr.,* **32,** 2571–2588.

Pichevin, T., and D. Nof, 1997: The momentum imbalance paradox. *Tellus,* **49A,** 298–319.

Qiu, B., M. Mao, and Y. Kashino, 1999: Intraseasonal variability in the Indo-Pacific throughflow and the regions surrounding the Indonesian seas. *J. Phys. Oceanogr.,* **29,** 1599–1618.

Sadourny, R., 1975: The dynamics of finite-difference models of the shallow-water equations. *J. Atmos. Sci.,* **32,** 680–689.

Yu, Z., and J. Potemra, 2006: Generation mechanism for the intraseasonal variability in the Indo-Australian basin. *J. Geophys. Res.,* **111,** C01013, doi:10.1029/2005JC003023.